Review of Scientific Instruments

The large helical device vertical neutron camera operating in the MHz counting rate range

Cite as: Rev. Sci. Instrum. **89**, 113509 (2018); https://doi.org/10.1063/1.5054818
Submitted: 04 September 2018 • Accepted: 02 November 2018 • Published Online: 21 November 2018

K. Ogawa, M. Isobe, T. Nishitani, et al.

The large helical device vertical neutron camera operating in the MHz counting rate range

K. Ogawa,[1,2,a)] M. Isobe,[1,2] T. Nishitani,[1] and T. Kobuchi[1]
[1]*National Institute for Fusion Science, National Institutes of Natural Sciences, Toki, Japan*
[2]*SOKENDAI (The Graduate University for Advanced Studies), Toki, Japan*

(Received 4 September 2018; accepted 2 November 2018; published online 21 November 2018)

In the currently performed neutral beam (NB) -heated deuterium plasma experiments, neutrons are mainly produced by a beam-plasma reaction. Therefore, time-resolved measurement of the neutron emission profile can enhance the understanding of the classical and/or anomalous transport of beam ions. To measure radial neutron emission profiles as a function of time, the vertical neutron camera (VNC) capable of operation with a counting rate in the MHz range was newly installed on the Large Helical Device (LHD). This is the world's first neutron camera for stellarator/heliotron devices. The VNC consists of a multichannel collimator, eleven fast-neutron detectors, and the digital-signal-processing-based data acquisition system (DAQ). The multichannel collimator having little cross talk was made from hematite-doped heavy concrete, which has a high shielding performance against both neutrons and gamma-rays. A stilbene crystal coupled with a photomultiplier having high-gain-stability in the high-count rate regime was utilized as a fast-neutron scintillation detector because it has a high neutron-gamma discrimination capability at high count rates. The DAQ system equipped with a field programmable logic controller was developed to obtain the waveform acquired with a 1 GHz sampling rate and the shaping parameter of each pulse simultaneously at up to 10^6 cps (counts per second). Neutron emission profiles were successfully obtained in the first deuterium campaign of LHD in 2017. The neutron emission profile was measured in tangentially co-injected NB-heated plasma with different magnetic axes (R_{ax}). The neutron counts became larger in the inward-shifted configuration, which was consistent with the total neutron rate measured by the neutron flux monitor. The radial peak position of the line-integrated neutron profile which changed according to R_{ax} showed that the VNC worked successfully as designed. The VNC demonstrated the expected performance conducive to extending energetic-particle physics studies in LHD. *Published by AIP Publishing.*
https://doi.org/10.1063/1.5054818

I. INTRODUCTION

Neutron diagnostics have been developed because neutron measurement is one of the key methods in order to obtain the fusion output power directly from a fusion burning plasma.[1] In deuterium plasmas, 2.45 MeV neutrons are produced as a result of the d(d,n)^{3}He reactions. The spatially resolved measurement of fusion neutron emission from the currently performed plasma experiment supports the theoretical modeling of the plasma, which preindicates the plasma behavior in a fusion reactor. In most of the currently performed neutral beam (NB) heated plasma experiments, neutrons are mainly created by the reactions between thermal plasma and beam ions. Therefore, neutron diagnostics have mainly been utilized to study the energetic ion behavior. The measurement of the neutron emission profile was reported for the first time in Princeton Large Torus (PLT) using nuclear emulsions in 1978.[2] The shot integrated neutron emission profile matched the theoretical model based on the Fokker-Planck equation under the total neutron emission rate of 10^{12} n/s. In the 1980s, the measurement of the time evolution of the neutron emission profile was possible using neutron cameras mainly composed of a multichannel collimator and fast-neutron detectors because the total neutron emission rate increased by more than a factor of four with the increase in the plasma performance.

Neutron cameras were installed and have been working since the late 1980s in large tokamaks. The vertical neutron camera (VNC) having the right cylinder type collimator was installed in the basement of the Tokamak Fusion Test Reactor (TFTR).[3,4] The multichannel collimator was made of brick and lead block stacked above the fast-neutron detectors. They used a zinc sulfide phosphor embedded in a hydrogenous polymer matrix scintillator (NE451) operated in the current mode. The neutron camera indicates that the peak of the line-integrated neutron emission profile agrees with the plasma axis as expected by transport code TRANSP.[3] Horizontal and vertical neutron cameras were installed in the Joint European Torus (JET).[5,6] Two multichannel collimators, made from barite-doped heavy concrete with a mass density of around 3.5 g/cm^3, are placed on the upper side and the outboard side of the plasma. The liquid scintillator (NE213) with the analogue-circuit-based pulse shape discrimination circuit was used and recently upgraded to the FPGA-based pulse shape discrimination circuit.[7] Tomography of the neutron emission profile is performed using both horizontal and vertical cameras.[8] Neutron cameras with six sight lines were installed on the outboard side of the JAERI Tokamak 60 Upgrade (JT-60U).[9] They used multichannel collimators made from polyethylene and lead.

a)Email: kogawa@nifs.ac.jp

The stilbene scintillator with the analogue-circuit-based pulse shape discrimination circuit was previously used. The circuit was upgraded to the flash ADC modules.[10] The energetic ion transport due to the energetic particle mode is observed with the neutron camera.[11] In middle size tokamaks, the neutron cameras are installed in FTU,[12] MAST,[13] KSTAR,[14,15] EAST,[16] HL-2A,[17] and MST[18] and are used to understand the energetic particle transport and losses.[19] In ITER, the installation of vertical and horizontal neutron cameras is planned.[20,21] In helical devices and stellarators, no neutron cameras have been installed because the neutron emission rate in previous experimental devices was too low to measure the neutron emission profile. The deuterium operation of the large helical device (LHD) makes it feasible to obtain time-resolved measurements of the neutron emission profile from the plasma because the expected neutron emission rate from the NB-heated deuterium LHD plasma is 10^{16} n/s order which is equivalent to the neutron emission rate of the deuterium operation of large tokamaks. The plan for installation of the VNC was initiated during the construction phase of the LHD.[22] The height of the multichannel collimator composed of polyethylene was studied by the MCNP5 code.[23] It was reported that a sharp peak of DD neutrons can be recognized when the collimator length is set to be 1.5 m. Through the study of the multichannel collimator design, progress was made in fast-neutron detection systems.[24] A multichannel collimator made of heavy concrete and a stilbene scintillation detector was suggested; however, the design of a fast-neutron detection system operating with 10^6 cps was not completed.[25] This paper describes the design and performance of the VNC stably operated with 10^6 cps, which is now used regularly to measure the time evolution of the neutron emission profile during LHD discharges.

II. DESIGN OF THE VERTICAL NEUTRON CAMERA

A. General outline

The VNC installed in the basement of the LHD torus hall sees the plasma from the lower side (Fig. 1). The VNC mainly consists of three parts: a multichannel collimator, fast-neutron scintillation detectors, and the digital-signal-processing-based data acquisition system. The VNC has a right cylinder collimator type similar to the neutron camera installed in TFTR and views the radial profile of neutron emission with eleven sight lines. The geometry ensures that each individual collimator channel has the same viewing efficiency. The distance from the plasma center to the multichannel collimator front and the fast-neutron detector are 5.5 m and 8.5 m, respectively. Eleven ICF70 ports aligned to the axis of the collimator were installed on the lower port of LHD. The thickness of the central part of the ICF70 flange is reduced to 2 mm in order to reduce the neutron scattering.

B. Multichannel collimator

The multichannel collimator is installed in the LHD torus hall concrete floor with a thickness of 2000 mm (Fig. 2). The hole created in the concrete floor has a rectangular shape. The size of the bottom opening is 1400 mm in depth (major radial direction) and 800 mm in width. The height of the multichannel

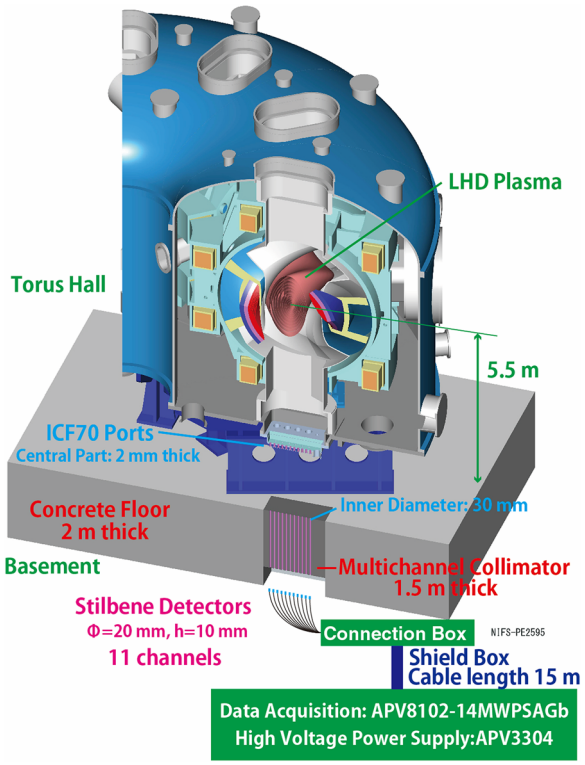

FIG. 1. Schematic drawing of LHD vertical neutron camera.

collimator was determined to be 1500 mm in order to implement sufficient shielding ability as evaluated using the neutron transport calculation.[23,24] The collimator support was made using angle bars made of SUS304A having a height of 250 mm, a width of 100 mm, and a thickness of 10 mm for fixing the vertical rib plate. The structure of the collimator support was designed based on a structural calculation. The collimator support is fixed with an M20 adhesive anchor, and the gap between the angle bars and the floor concrete is filled by shrinkage-compensating mortar in order to avoid water and concrete falling to the understructure. The multichannel collimator is made using the hematite (Fe_2O_3)-doped heavy concrete. The mass density of heavy concrete is 3.5 g/cm^3, which is almost the same as the mass density of the heavy concrete used for the multichannel collimator of the JET neutron camera. We used 210 kg of water, 380 kg of cement, 2100 kg of hematite with a particle size of 2 mm and 3700 kg of hematite with a particle size of 20 mm. The composition of heavy concrete is shown in Table I. Note that the reason for using the heavy concrete is that the heavy concrete collimator has better performance in reducing unwanted gamma-rays compared with collimators made of polyethylene and lead according to the Monte Carlo neutron and gamma-ray transport calculation.[24]

The collimator consists of 3 sub-sections of 500 mm high stainless steel (SUS304A) pipes embedded in heavy concrete. The three collimator units are stacked on the collimator support, and then the gap between collimator units and the floor concrete is filled with heavy concrete. Here, we caulked the small gap between collimator unit and collimator support to avoid water leakage. The reason for making three collimator units is in order to avoid the bending of relatively long stainless steel pipes due to the high pressure from the heavy

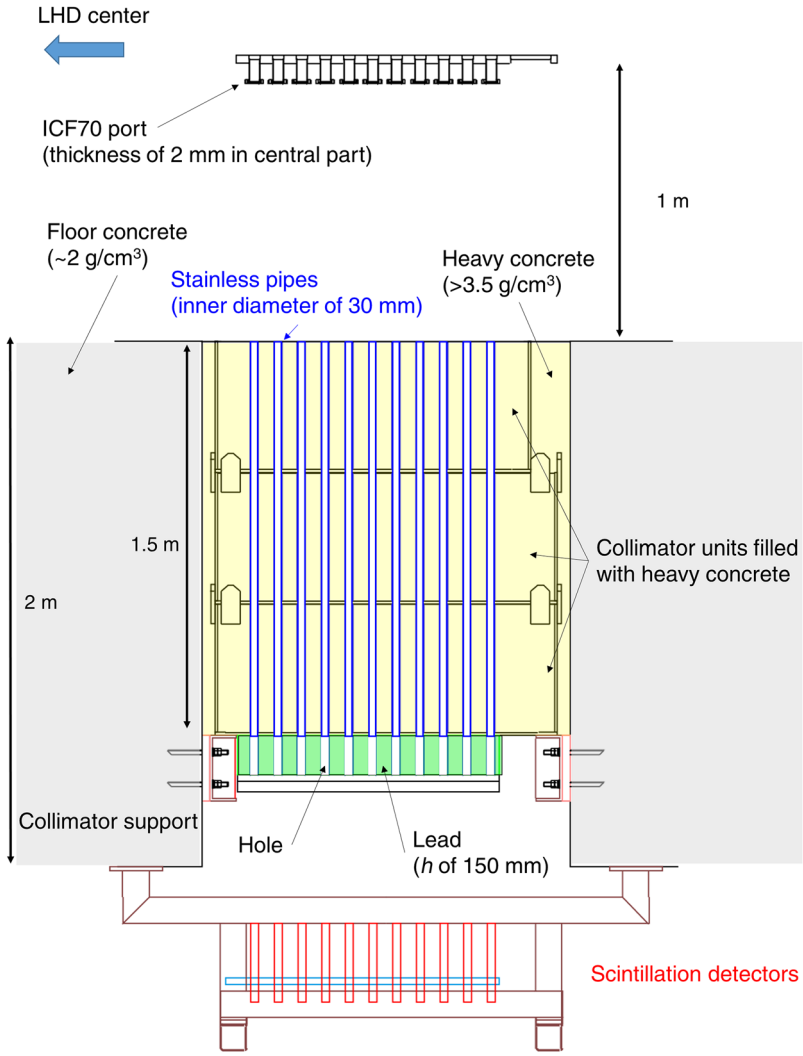

FIG. 2. Schematic of the ports, the multichannel collimator, and the detector support of LHD VNC.

concrete. Here, the size of the collimator unit placed on the top is slightly smaller than that of the others in order to obtain easier access to the lower region during the concrete placing work. The total weight of the heavy concrete used for the multichannel collimator is approximately seven tons. In addition to the heavy concrete collimator, lead with a thickness of 150 mm (30 sheets of t of 5 mm lead plate) is placed under the heavy concrete collimator in order to reduce the unwanted gamma-ray. Note that holes with a diameter of 30 mm are made in the lead sheets along the sight lines to avoid the neutron scattering. The VNC has eleven sight lines whose inner diameter is 30 mm aligned radially. A sight line is placed at each R of 3.36 m, 3.45 m, 3.54 m, 3.63 m, 3.72 m, 3.81 m, 3.90 m, 3.99 m, 4.08 m, 4.17 m, and 4.26 m. The distance between the centers of two sight lines is 90 mm. Note that the inner diameter of the sight line can be changed to 10 mm or 20 mm using an additional stainless steel pipe with the length of 500 mm. It should be pointed out that the relatively short length of the additional stainless pipe is to avoid having a smaller pipe become stuck inside a larger pipe. Fast-neutron detectors are placed at the bottom of the multichannel collimator. The support of neutron detectors is designed to accept a supporting weight of 500 kg. The cross talk of the multichannel collimator is experimentally obtained by using an intensive ^{252}Cf neutron source. The experimental results indicate that the cross talk of the multichannel collimator is approximately 1%.[26]

Figure 3 shows the sight line of the VNC together with the poloidal cross section of the plasmas having the magnetic axis positions (R_{ax}) of 3.60 m and 3.90 m. The figure shows that the VNC is designed to cover of the entire plasma region and obtain the information about the plasma axis position. Here, the sight line with R of 4.26 m is designed in order to obtain the

TABLE I. Weight ratio of heavy concrete material.

Chemical composition	Weight ratio (%)
H_2O	3.3
SiO_2	1.2
Al_2O_3	0.28
Fe_2O_3	91
CaO	3.8
MgO	0.084
SO_3	0.17
Na_2O	0.015
K_2O	0.022
Cl	0.000 29

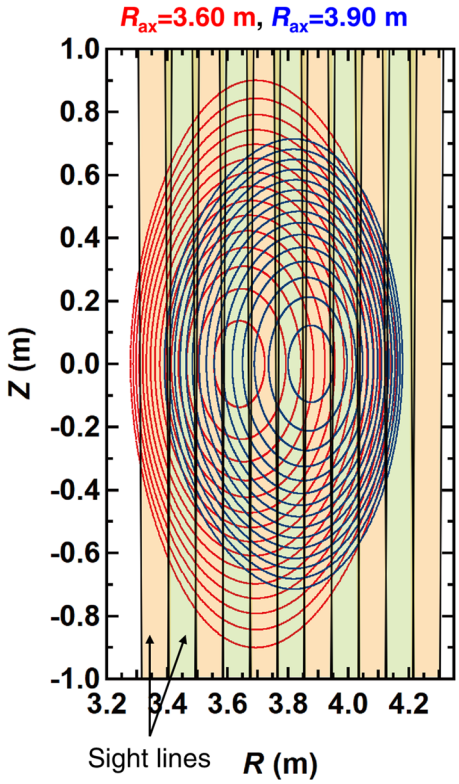

FIG. 3. Sight lines of VNC and poloidal cross section of plasma with R_{ax} of 3.60 m and 3.90 m with zero beta. The diameter of each sight line is 88 mm at Z of −0.9 m and 110 mm at Z of 0.9 m.

background counts. The plasma visible region through sight line is approximately a cylinder with an 88 mm diameter at the bottom of the plasma and a 110 mm diameter at the top of the plasma for the central cord (R of 3.63 m), and the volume of the visible region is 0.05 m^3.

C. Fast-neutron detection system

The block diagram of the fast-neutron detection system is illustrated in Fig. 4(a). We choose a stilbene scintillator directly coupled with the PMT (H11934-100-10MOD[27] with a 3 m cable) having high gain stability as a fast-neutron detector. The typical rise and transit time of the PMT are 1.3 ns and 5.8 ns, respectively. The signal from the fast-neutron detector is directly fed into the data acquisition system. The length of the co-axial cable (3D-FB[28]) from the detector to the data acquisition system is 18 m. The length of the cable is decided by the possible locations for installing the Fast-neutron detection system and the effect of the cable length on the signal. We evaluated the effect of the cable length on the pulse height and width using an LED emitting green light. Here, the pulse width of the LED light is 20 ns. The data acquisition system should be placed away from the machine to prevent radiation damage of the data acquisition system. However, the long cable causes a reduction in the signal height and the broad signal. Therefore, the effect of the cable length on the pulse signal was investigated. Figure 4(b) shows the pulse height and width measured by an oscilloscope (DPO 7104C,[29] Tektronix) as a function of the cable length. The pulse height gradually

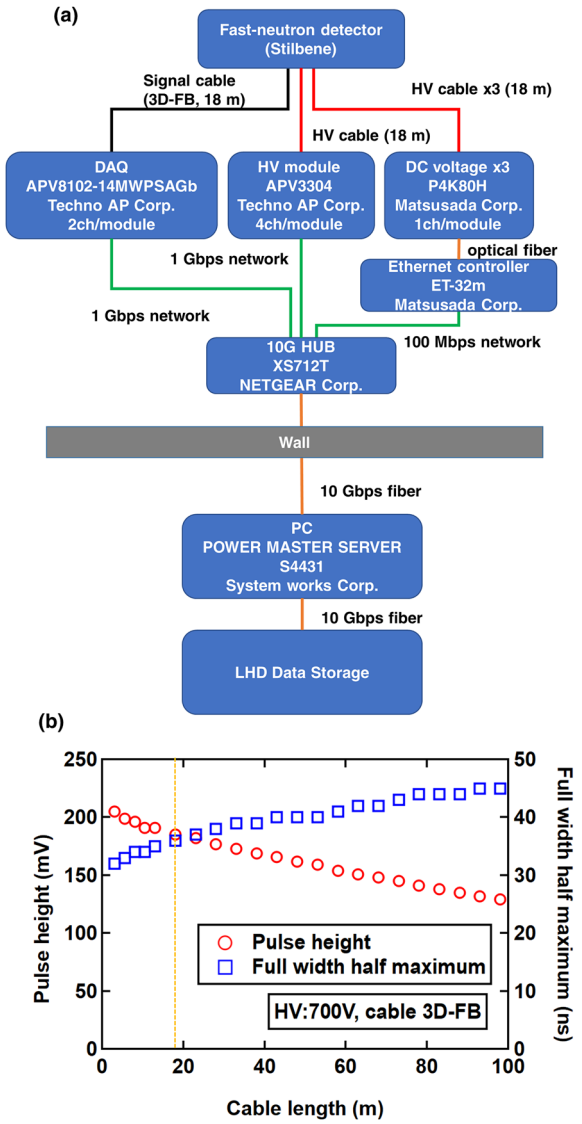

FIG. 4. (a) Electronic schematic of VNC. All the electrical components are externally controllable. (b) Pulse height and pulse width as a function of cable length.

decreases and the pulse width gradually expended with the increase in the capacitance of the cable, as expected. The pulse height decreases by 25% at the cable length of around 50 m, and the pulse width becomes 30% wider at the cable length of around 40 m compared with a 3 m cable (no cable extension). It is found that on the VNC the pulse height decreases by 10% and the pulse width becomes wider by 11% with an 18 m cable compared with a 3 m cable. On the other hand, the pulse height decreases by 40%, and the pulse width becomes wider by 50% with a 100 m cable. The data acquisition system for the VNC is placed on the basement level of the torus hall (cable length of 18 m) rather than in the data acquisition room located outside of the torus hall (100 m) because 40% smaller means that the signal to noise ratio becomes a 40% less and a 50% wider signal induces a 50% higher pile up rate. The data acquisition system (APV8102-14MWPSAGb,[30] Techno AP) composed of the fast digitizer, a leading edge technology field programmable logic circuit, and synchronous dynamic random access memory (SDRAM) is developed for the LHD VNC.

High voltage is applied using an externally controllable high voltage power supply with a logging function (APV3304,[31] Techno AP). We can obtain the information of both applied voltage and supplied current every 1 ms to monitor the gain variation of the PMT. The maximum voltage and current of APV3304 are 1 kV and 4 mA, respectively. In addition to the primary high voltage module, external DC power supplies (P4K80H,[32] Matsusada Precision) are additionally prepared in order to suppress the gain shift of the PMT in the high counting rate regime. The maximum voltage, current, and power of P4K80H are 320 V, 0.5 A, and 80 W, respectively. The Ethernet outputs of these modules are gathered to the high-speed Ethernet hub (XS712,[33] NETGEAR Corp.) equipped with an SFP + port. The SFP + port is connected to the data acquisition PC through a 10 Gbps network. Because the minimum operation interval of the LHD is approximately 3 min and the maximum stored data of the data acquisition system (DAQ) is 11 GB, the required average transfer rate of the data acquisition system is more than 500 Mbps. Therefore, we choose the 10 Gbps network for the data transfer. To acquire such large data with high speed, we choose a relatively high performance data acquisition server equipped with Xeon E5-2603v3 × 2 CPUs, 32 GB DDR4 ECC Registered memory, Intel Ethernet SFP+, and SSD (SSDSC2KW240H6X1) × 3 RAID0. The specification of each component in detail will be described in Sec. III.

III. EXPERIMENTAL SYSTEM

A. Magnetic shield for fast-neutron detector

The neutron detector must work under a relatively strong magnetic field environment; however, the effect of neutron scattering due to the magnetic shield should be reduced. The goal was to design the magnetic shield surrounding the PMT without front and back sides in order to reduce the neutron scattering. The fast-neutron detector shown in Fig. 5 is composed of the magnetic shield, the stilbene scintillator, and the photomultiplier. Because the photomultiplier (PMT) is sensitive to the magnetic field, we need the magnetic shield in order to reduce the magnetic field strength to an acceptable value. The acceptable magnetic field for the PMT used for the LHD VNC is approximately 0.05 mT. Figure 6(a) shows the profile of the magnetic field strength at the standard configuration of the LHD experiment at R of 3.60 m. Here, the toroidal magnetic field strength (B_t) is 3 T and R_{ax} is 3.60 m, and Z = 0 corresponds to the plasma axis position. The figure shows that the magnetic field strength of the fast-neutron detector position at Z = 8 m is around 12 mT in the radial direction and 6 mT in the vertical direction. It is notable that the toroidal magnetic field component is negligibly small compared with the radial magnetic field component. We designed the magnetic shield with a 1 mm thickness of Permalloy C surrounded by a 10 mm thickness of SS400 using the finite element method. The length of the magnetic shield is 300 mm, and the photomultiplier tube is located at the center of the magnetic shield. We designed a relatively long magnetic shield so that no magnetic shield component is located on the front and the back of the fast-neutron detector in order to avoid

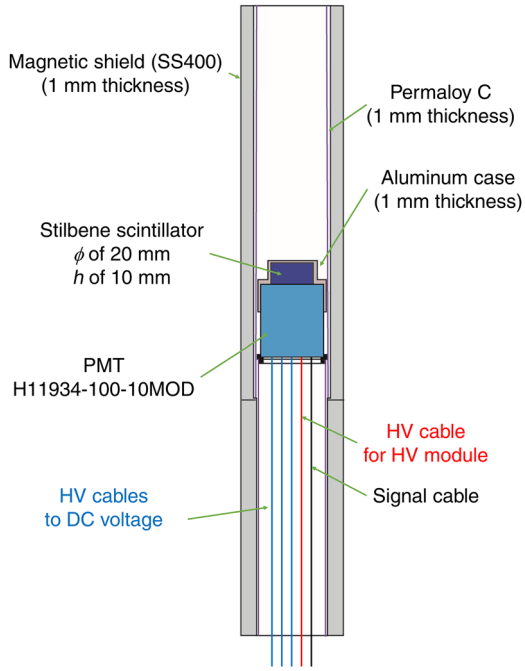

FIG. 5. Schematic drawing of the fast-neutron detector.

the scattering of fast-neutron due to the magnetic shield. We should keep in mind that the weight of the magnetic shield is approximately 10 kg. The performance of the magnetic shield

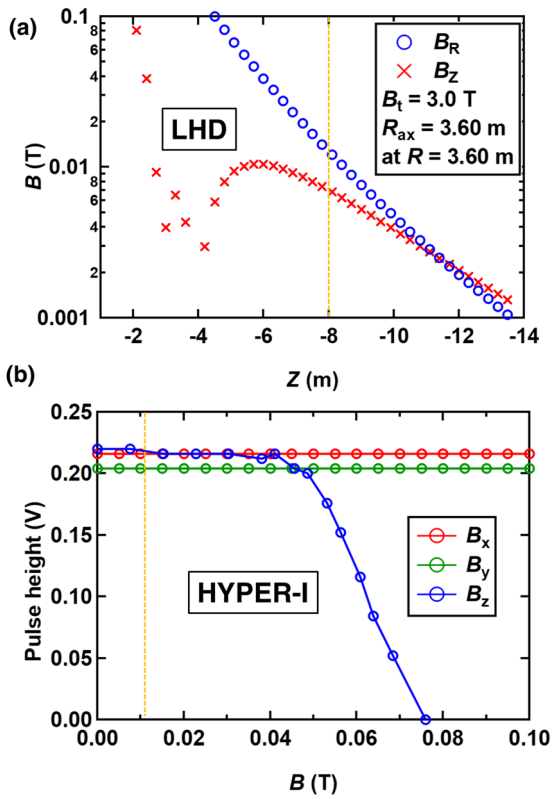

FIG. 6. (a) Typical profile of magnetic field strength at the vertically elongated cross section in LHD where B_t, R_{ax}, Z, and R represent the toroidal magnetic field strength, the plasma major radius, the height from the plasma plane, the major radius from the machine center, respectively. The dashed line shows the location of fast-neutron detectors. (b) Test of the magnetic shield in HYPER-I. The dashed line shows the magnetic field strength at the fast-neutron detector position. The magnetic shield has sufficient performance as designed.

was checked by an experiment using a light emitted diode (LED) in the magnetic field produced by HYPER-I.[34] HYPER-I is the linear high-density plasma device which can produce a linear magnetic field up to 250 mT. The PMT surrounded by magnetic shield was placed parallel/perpendicular to the axis of HYPER-I. An LED fixed in front of the PMT emits a light using a function generator (WF1946,[35] NF Corporation) with a pulse rate of 100 Hz and pulse width of 30 ns. We changed the magnetic field strength and recorded the pulse height of the PMT signal measured by an oscilloscope (DPO 7104C, Tektronix). The pulse height as a function of the magnetic field strength is shown in Fig. 6(b). Here, z is defined along the central axis of the PMT, and x and y are perpendicular to the z axis. The dependence of the pulse height as a function of the magnetic field strength shows that the pulse height stays constant in the B_x and B_y cases, whereas the pulse height decreases from B of 0.04 T in the B_z case. The design of a magnetic shield having minimal neutron scattering effect and working in the VNC position (B_R of around 12 mT and B_Z of 6 mT) was completed.

B. Gain stability of PMT in high-counting rate region

The understanding on the characteristics of the PMT in the high counting rate regime is one issue for stable operation of the neutron measurement, especially in the neutron and gamma-ray discrimination. In JT60-U, the gain shift of the PMT caused a disturbance on the neutron and gamma-ray discrimination plot.[36] The goal of the PMT development is no gain shift in the MHz pulse rate region. The PMT used for the fast-neutron detector of the LHD VNC has a metal channel dynode structure and consists of twelve stages. The maximum applied high voltage and typical gain are −1000 V and 4.8×10^5, respectively. High voltage cables and 0.01 F capacitors are connected to the last three dynodes of the PMT. Each high voltage cable is connected to an external voltage module. In the high counting rate region, these external DC power supplies supply the current in order to sustain the high voltage in the latter phase of the dynodes for suppressing gain variation in the high counting rate condition. The gain stability of the PMT was checked by using two LED lights emitting green light. The experimental setup is shown in Fig. 7(a). Two LEDs were fixed in front of the PMT placed in a dark room. One LED called LED1 emitted a light with 100 Hz, whereas the frequency of the other LED called LED2 was changed from 300 Hz to 10^6 Hz. We measured the pulse height of the PMT signal created by LED1 light by an oscilloscope (DPO 7104C, Tektronix). Here, the pulse height and width created by LEDs are around 200 mV and 30 ns, respectively, in the case of a high voltage of 700 V, which is similar to the pulse height of a 2.45 MeV neutron signal of the fast-neutron detector. Figure 7(b) shows the pulse height created by LED1 as a function of the pulse rate of LED2. The pulse heights in the case of the high voltages of 700 V and 800 V are 200 mV and 600 mV, respectively. The gain of the PMT at 700 V and at 800 V is 4.0×10^4 and 1.5×10^5, respectively. It is worth noting that the gain shift occurred at a different pulse rate in each case. The gain shift of the PMT occurred depending on the ratio of the signal current on the dynode current. When the signal current becomes not negligible with respect to the dynode current, a gain shift occurred due to the decrease in the voltage between dynodes of the PMT. The signal current of the PMT increases nonlinearly with high voltage, whereas the dynode current increases linearly with the high voltage. Therefore, the saturation level becomes lower in the 800 V case compared with the 700 V case because the ratio of the signal current on the dynode current is higher. In the case of a high voltage of 700 V, without external DC power supplies, the pulse height increases from around the pulse rate of 10^5 Hz and then decreases starting from 3×10^5 Hz, whereas the pulse height is almost constant regardless of the pulse rate of LED2 with external DC power supplies. In the case of a high voltage of 800 V, without external DC power supplies, the pulse height increases at a pulse rate of LED2 of 10^3 Hz and then decreases monotonically with respect to the pulse rate of LED2, whereas the pulse height is almost constant irrespective of the pulse rate of LED2 with external DC power supplies. The experimental results show that the external DC power supplies work successfully to suppress the gain variation, and the gain of the fast-neutron detector is stable under the pulse rate of 10^6 Hz. The PMT suitable for the stilbene fast-neutron detector stably operated at a 10^6 pulse rate without gain variation was developed.

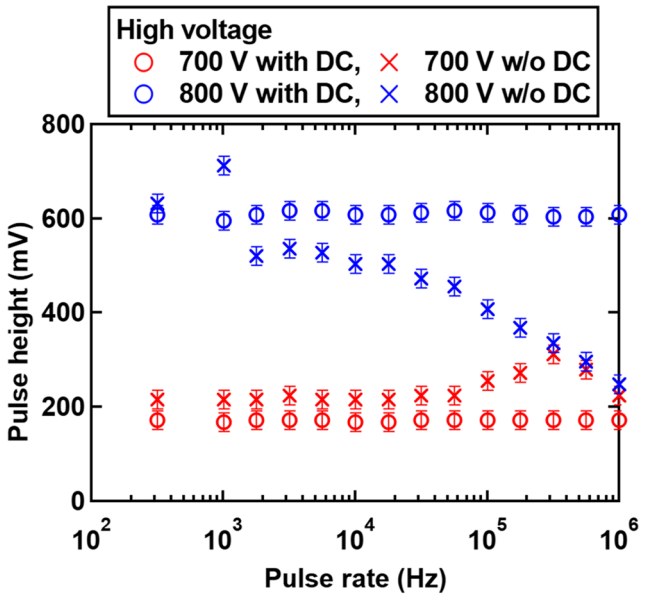

FIG. 7. Result of gain stability. The gain of PMT is not changed even at 10^6 cps with external DC power supplies.

C. Digital signal processing unit

The DAQ system (APV8102-14MWPSAGb) for the VNC is newly developed by combining a high-speed sampling rate analog to digital converter (1 GHz sampling, 14 bits and 2 or 6 V_{pp}) and a field programmable logic circuit [Fig. 8(a)] in order to accept the superior performance of fast-neutron detector operating in the 10^6 pulse rate regime. Figure 8(b) is a block diagram of the DAQ board. The signal acquired by the high speed ADC is transferred to the FPGA. The FPGA judges whether the signal is above the threshold value.

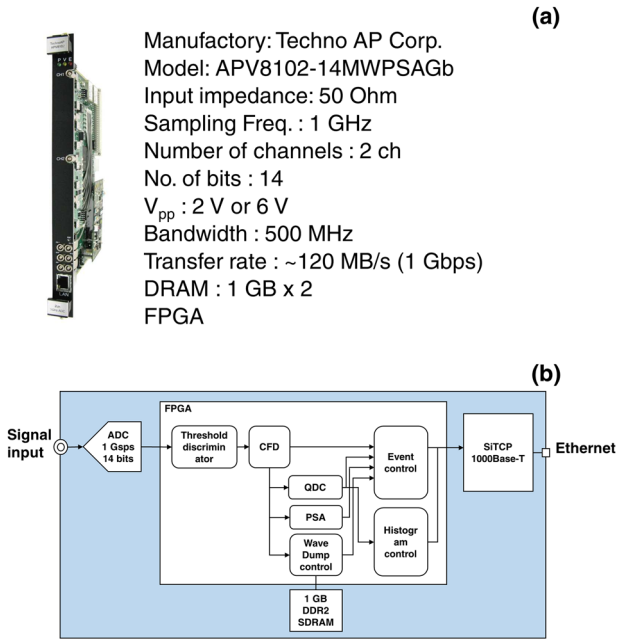

FIG. 8. (a) Specification of DAQ for LHD VNC. (b) Electronic schematic of the DAQ. The data are stored in the internal memory and transferred after the discharge.

If the signal exceeds the threshold value, the time stamp is recorded by using the constant fraction discriminator (CFD) function. Then, signal integrations Q_{total} and Q_{long} are calculated. At the same time, the raw waveform consisting of 64 points is stored in the 1 GB SDRAM. After the discharge, all the data are transferred to a PC through the Ethernet. Here, the data size of each pulse is 144 bytes. Therefore, the expected data transfer rate at the 10^6 cps counting rate is ~1.2 Gbps per channel. Then we choose DDR2 SDRAM because of its high data transfer rate of more than 3 Gbps. The DAQ only stored meaningful pulses. The acquisition time is not limited by the duration of the acquisition but by the number of pulses. The maximum number of pulses stored in the board is designed to be 3×10^6 per channel because of the maximum expected neutron counts on an LHD discharge (10^6 cps $\times$ 3 s).

IV. CHARACTERISTICS OF FAST-NEUTRON DETECTION SYSTEM

A. Optimal t_{fast} for pulse shape discrimination

Pulse shape discrimination (PSD) is performed using the expression PSD = $Q_{\text{long}}/Q_{\text{total}}$. Here, Q_{total} represents integration of the signal from the beginning to the end of the stored waveform of 64 ns length, whereas Q_{long} represents the integration of the signal from an arbitrary time in the middle of the signal, t_{fast}, to the end. As shown in Fig. 9(a), the neutron induced signal has a longer decay time, and then the PSD becomes larger compared with the PSD of the gamma-ray induced signal. We evaluated the pulse shape discrimination ability using a ^{252}Cf neutron source in order to obtain the optimal t_{fast}. Figure 9(a) shows the typical waveform

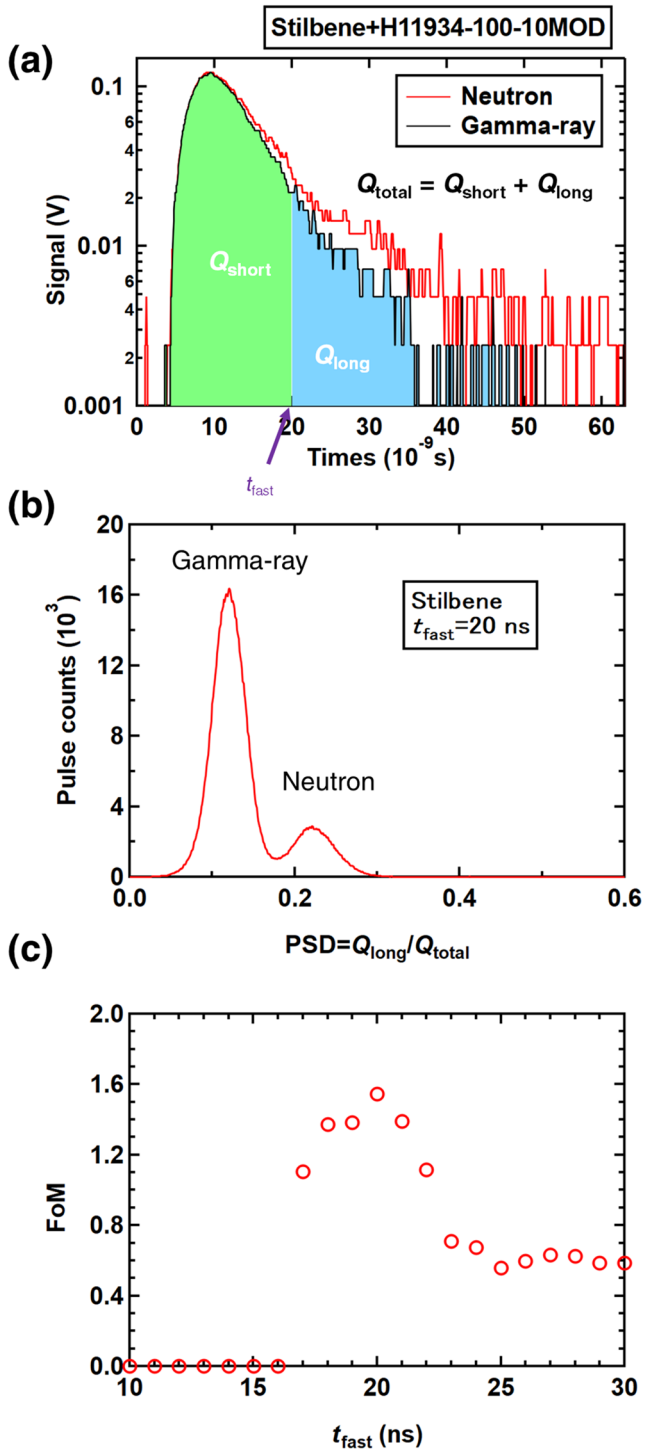

FIG. 9. (a) Typical signal of the fast-neutron detector induced by fast-neutron and gamma-ray. The decay time of the signal is longer in the fast-neutron case compared with gamma-rays. (b) Typical one-dimensional histogram of pulse shape discrimination for stilbene detector. (c) Pulse shape discrimination ability as a function of t_{fast}. The highest FoM is obtained at a t_{fast} of around 20 ns.

acquired by APV8102-14MWPSAGb. Figure 9(b) shows the pulse shape discrimination result of stilbene detectors at t_{fast} of 20 ns. We surveyed the pulse shape discrimination ability as a function of t_{fast}. Here, we used the Figure of Merit (FOM) as an index of the pulse shape discrimination ability. The FOM is defined as FOM = [PSD_peak

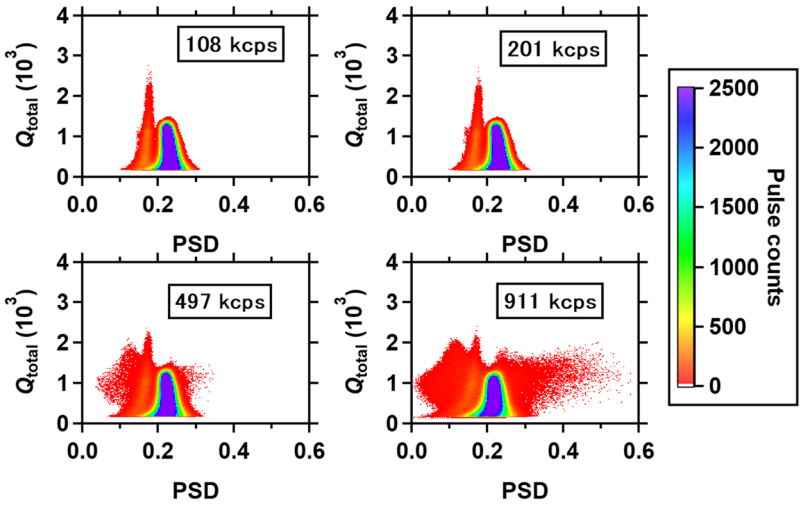

FIG. 10. Two dimensional pulse shape discrimination plots in different counting rates obtained in the FNS. Here, PSD = Q_{long}/Q_{total}. The map appears to be stable regardless of the counting rate.

(neutron) − PSD_peak(gamma-ray)]/[FWHM(neutron) + FWHM(gamma-ray)], where FWHM indicates the full width at half maximum. A non-zero FOM appears from t_{fast} of 17 ns, has a peak around 20 ns, and decreases from t_{fast} of 22 ns. It should be pointed out that no FOM was obtained when t_{fast} was less than 17 ns because only one peak appeared. Therefore, it is found that the optimal t_{fast} for this fast-neutron detector is around 20 ns.

B. PSD capability in high counting rate

The DD neutron measurement using the fast-neutron detector is performed using an accelerator-based neutron generator on the Fast Neutron Source (FNS) in the Japan Atomic Energy Agency.[37] The DD neutrons are generated due to the deuteron beam and the deuterium target reaction. The typical neutron emission rate from the target is 10^9 neutrons per second. We used an x-axis stage (KXL06300,[38] Suruga Seiki CO., LTD.) in order to change the neutron flux at the detector position by changing the distance from the target to the detector. Note that the neutron flux at the detector position is from 2.5×10^6 cm^{-2} s^{-1} to 2.2×10^7 cm^{-2} s^{-1}. The fast-neutron detector is placed in front of the DD neutron target. The energy of the DD neutron is around 3 MeV. Figure 10 shows the two dimensional pulse shape discrimination plot at the pulse counting rate of 108 kcps–911 kcps. Here, the total number of pulses of each run is 3×10^6. Two peaks corresponding to the neutron and gamma-ray are clearly separated. It is important to note that the pulse shape discrimination map does not change as expected from the characteristics of the PMT gain stability reported in Sec. II B. Here, we can see several points on the left- and the right- hand side of the two dimensional plot; this is due to the pile-up of pulses. The number of these plots increases with the increase in the counting rate as expected by the simple pile up calculation $[n/(1 - nt_{pulse})]$: n and t_{pulse} represent the counting rate of the pulse measured by the ADC and the total width of the pulse, respectively. The larger PSD is obtained when the second pulse comes after t_{fast}, whereas when the second pulse is coming before t_{fast}, the smaller PSD is obtained. The number of pulses acquired by the DAQ as a function of the expected pulse counting rate evaluated by the neutron flux is shown in Fig. 11. Here, we compared three different digitizers: DT5751[39] CAEN, NI5772[40] + PXIe-7962R[41] National Instruments, and APV8102-14MWPSAGb Techno AP. DT5751 has 10 bits, 1 GHz, and 1 V_{pp}, and only online analysis based on Q_{long} and Q_{short} is possible. NI5772 + PXIe-7962R reported in Ref. 23 has 12 bits, 1.6 GHz, equipped with 512 DDR2 SDRAM memory, and either online analysis or offline analysis (stored waveforms) is possible. It is should be emphasized that those three DAQs acquire the periodic pulses with 10^6 pulses per second without any loss of pulses. The loss of pulses occurred when the expected counting rate was around 8×10^5 cps. Here, the counting rate of the ADC compensates with simple pile-up theory. The pulse loss ratio of DT5751, NI5772 + PXIe-7962R, and APV8102-14MWPSAGb at 10^6 cps are around 12%, 16%, and 8%, respectively. It is found that the highest counting resistance among these three DAQs APV8102-14MWPSAGb.

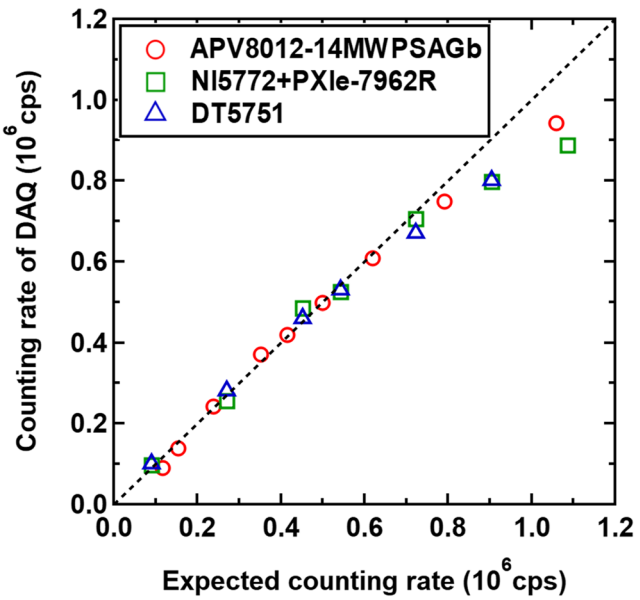

FIG. 11. Pulse counting rate obtained with DAQ as a function of expected counting rate evaluated by the neutron flux at the detector position in the FNS. The counting loss ratio of APV8102-14MWPSAGb is minimum among three DAQs.

C. Detection efficiency and detector response

The detection efficiency and the detector response of the fast-neutron detector are obtained at the Fast Neutron Laboratory (FNL)[42] of Tohoku University, at FNS, and at the Intense 14 MeV Neutron Source Facility (OKTAVIAN)[43] of Osaka University. We used the p-Li reaction in order to produce neutrons having an energy of 1.3 MeV in FNL, d-D reaction for 3 MeV neutrons in FNS, d-D reaction for 4.5 MeV–5.7 MeV neutrons in FNL, and d-T reaction for 14 MeV neutrons in OKTAVIAN. Figure 12(a) shows the pulse height spectra of the fast-neutron detector. Note that the threshold value in the case of a neutron energy of 1.3 MeV and the threshold value in the other case are 10 mV and 30 mV, respectively. The lower threshold value in the case of the neutron energy of 1.3 MeV is for observing the response of the lower energy neutrons. Here, pulse height is evaluated by the waveform data. The pulse

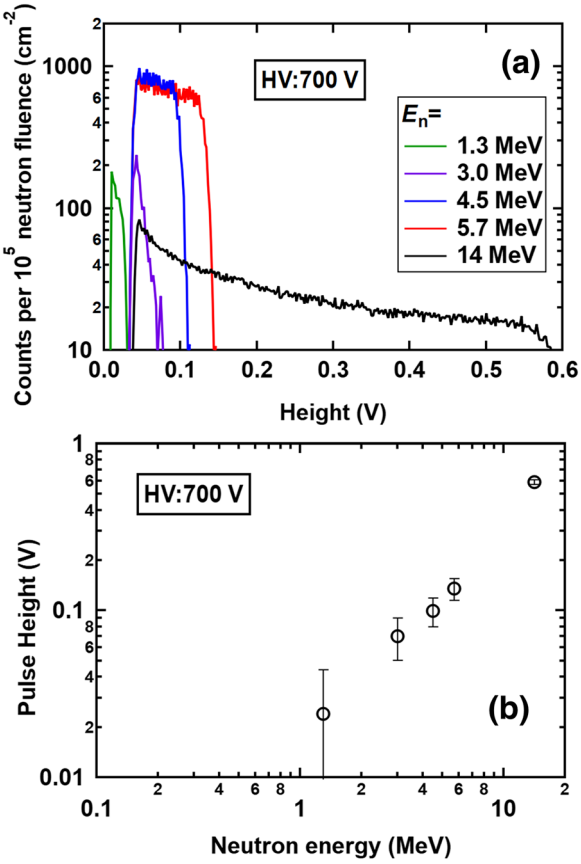

FIG. 12. (a) Pulse height spectra obtained at the neutron energy of 1.3 MeV, 3.0 MeV, 4.5 MeV, 5.7 MeV, and 14 MeV. (b) The maximum pulse height as a function of neutron energy. The pulse height monotonically increases with neutron energy as expected.

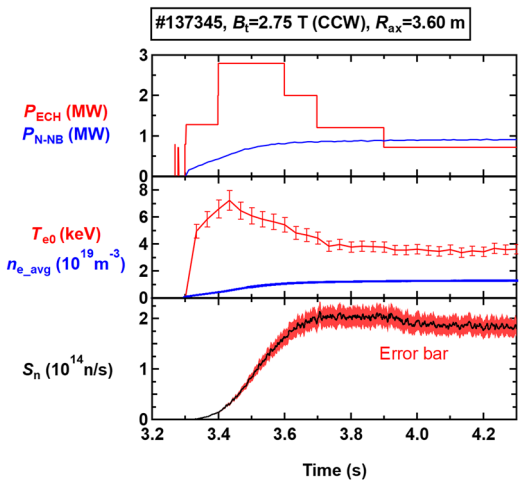

FIG. 13. Typical time trace of electron cyclotron heated (ECH) and negative-ion-based neutral beam (N-NB) injected plasma discharge.

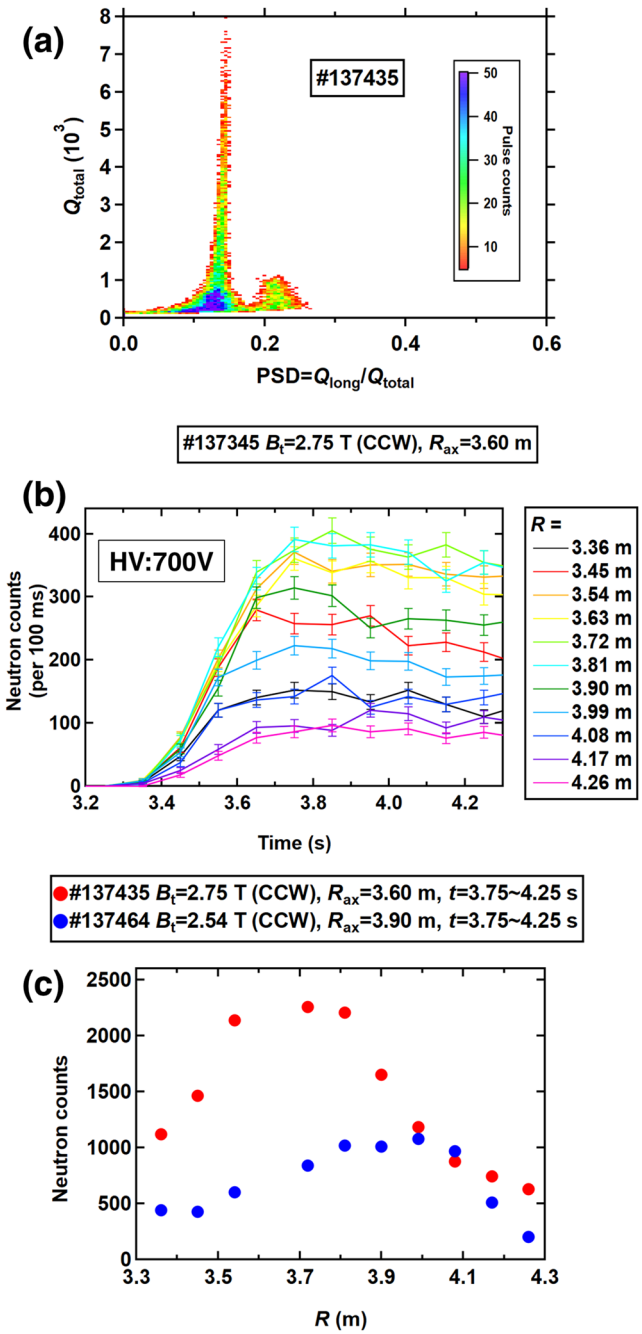

FIG. 14. (a) Typical two-dimensional pulse shape discrimination plot obtained in the LHD experiment. (b) Typical time traces of the line-integrated neutron emission profile. (c) Typical line-integrated neutron emission profile obtained at R_{ax} of 3.60 m and 3.90 m. Number of neutron count decreases with the outward shift of R_{ax} which is consistent with the total neutron emission rate measurement. The peak position of the profile shifted outward with R_{ax} as expected.

height becomes larger with the increase in the neutron energy, as expected. Figure 12(b) shows the maximum pulse height as a function of neutron energy. The plot shows that we can measure fast neutrons having an energy of around 2 MeV if the threshold value is set to be 30 mV. We evaluated the counting efficiency using an indium foil in the FNS experiment. In this experiment, the indium foil was placed in front of the stilbene detector and the time evolution of the neutron emission rate was evaluated by a beam current monitor. Here, the distance between the deuterium target and the stilbene detector was 10 cm. It was found that the counting efficiency of the stilbene detector is 0.06 counts/neutron/cm^{-2}, for 3 MeV neutrons with high voltage of 700 V and threshold setting of 30 mV.

V. TYPICAL DATA OF THE LHD EXPERIMENT

Measurement of the time evolution of the neutron emission profile is performed in the LHD deuterium operation (Fig. 13). In this discharge, B_t is 2.75 T and R_{ax} is 3.60 m. Electron cyclotron heating and a negative-ion-based NB injection are started at the time t = 3.3 s. Thomson scattering diagnostics[44] measure the central electron temperature, and the line-averaged electron density is measured by an interferometer.[45] The total neutron emission rate (S_n) measured by the absolutely calibrated neutron flux monitor[46] gradually increases due to NB injections. Figure 14(a) shows the pulse shape discrimination result of channel 4 (R of 3.63 m). The two peaks are clearly separated at a PSD of 0.175. In this discharge, the number of neutron counts is 3500, whereas the number of gamma-ray counts is 17 000. The time evolution of the line-integrated neutron profile shows almost a similar trend with S_n, as shown in Fig. 14(b). The neutron emission profiles are obtained in different R_{ax} configurations [Fig. 14(c)]. As R_{ax} shifts outward, neutron counts decrease due to the decrease in S_n. In addition, the peak of the line-integrated neutron emission profile shifts outward with R_{ax}, as expected. We showed that the VNC is installed with the desired performance. The VNC will be a powerful tool to measure the neutron emission profile in LHD.

VI. SUMMARY

The vertical neutron camera characterized by high-counting rate capability is developed for LHD deuterium operation in order to understand the beam ion behavior. A multichannel collimator was constructed with hematite-doped heavy concrete. The magnetic shield is designed based on a finite element method by considering the magnetic field strength at the VNC position. We experimentally showed that the magnetic shield is manufactured according to the design requirements. The fast-neutron detector composed of a stilbene scintillator characterized by high pulse shape discrimination ability coupled with the PMT characterized by high gain stability equipped with external DC power supplies for further improved gain stability was installed. The test of the high gain stability of the PMT using an LED shows that external DC power supplies are effective for suppressing the gain variation, and the gain of the PMT is constant up to the pulse rate of 10^6 Hz. The DAQ composed of the fast ADC and the novel logic circuit realized in the FPGA enable us to obtain data needed for online and offline analysis simultaneously. The neutron measurement was performed on accelerators using p-Li, d-D, and d-T reactions. It is found that the two dimensional pulse shape discrimination map does not change even in the 10^6 cps region. The counting loss of the pulse under the 10^6 cps is 8%, which is the smallest value compared with other digitizers like DT5751 and NI5772 + PXIe-7962R. The response of the fast-neutron detector shows that the detector can measure the neutron energy from around 2 MeV when the discrimination level is set to be 30 mV. Initial measurement of the line-integrated neutron emission profile was performed in LHD deuterium operation in order to check the expected performance of the VNC. The time-resolved neutron emission profile has a time trend similar to the total neutron emission rate. The typical neutron, gamma-ray ratio is 1:5 for the central channel. The measurement of the neutron emission profile at R_{ax} of 3.60 m and of 3.90 m shows that the peak of the line-integrated neutron emission profile shifts according to the R_{ax} position as expected.

ACKNOWLEDGMENTS

This research was supported by NIFS Collaboration Research Programs (No. KOAH033), by the LHD Project Budget (Nos. ULHH003, ULHH034, ULHH802, and ULGG801), and Japan/U.S. Cooperation in Fusion Research and Development. One of the authors, K. Ogawa, is pleased to acknowledge the assistance of LHD Experiment Group for assistance in installation and operation of the VNC; K. Ochiai and the FNS team of National Institutes for Quantum and Radiological Science and Technology, M. Miwa, S. Matsuyama, and the FNL team of Tohoku University, and I. Murata of the OKTAVIAN team of Osaka University for assisting in obtaining the neutron detector response; H. Tomita and A. Uritani of Nagoya University, S. Conroy, L. Giacomelli, and V. Kiptily of Culham Centre for Fusion Energy, A. L. Roquemore and the late D. S. Darrow of Princeton Plasma Physics Laboratory, G. Q. Zhong of the Chinese Institute of Plasma Physics, and T. Itoh of Kitano Manufacturing Corp. in discussing the design of a multichannel collimator and detectors; T. Honda and M. Goto of G-tech Corp. in discussing the PSD ability of the scintillator; A. Okada of Hamamatsu Photonics K.K. in providing background knowledge of the photomultiplier; T. Takada of National Institute of Technology, Ariake College and S. Yoshimura of National Institute for Fusion Science in assisting with PMT test using LED; E. Takada of National Institute of Technology, Toyama college, M. Riva, D. Marocco, B. Esposito, B. Francesco of the Italian National Agency for New Technologies, Energy and Sustainable Economic Development in discussing the FPGA logic; and Y. Endo, F. Watanabe, and Y. Arai of Techno AP for joint development of the FPGA circuit.

APPENDIX: MULTICHANNEL COLLIMATOR FOR LHD VNC

Three multichannel collimator units used for LHD VNC are shown in Fig. 15(a). The weight of each unit is approximately 2 tons. Figure 15(b) shows the multichannel collimator

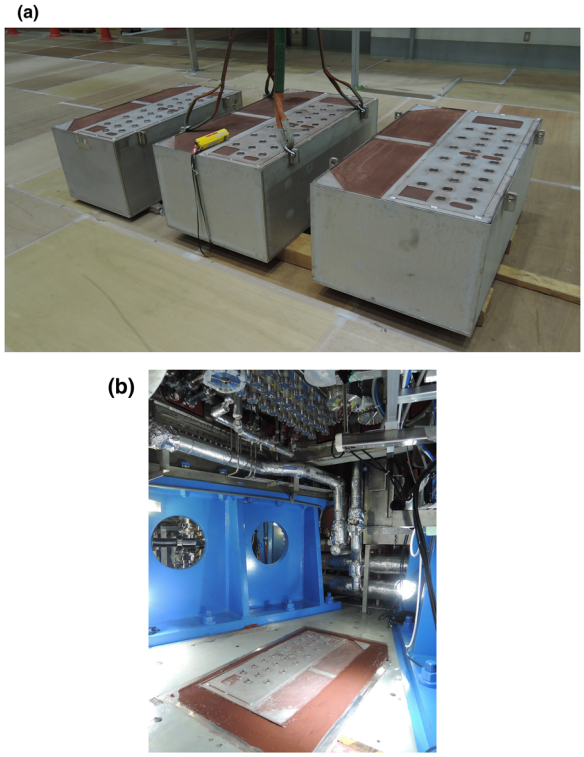

FIG. 15. (a) Three multichannel collimator units. (b) The multichannel collimator made in the LHD torus hall.

installed in the LHD torus hall. Total weight of multichannel collimator is approximately 7 tons.

[1] O. N. Javis, Plasma Phys. Controlled Fusion **36**, 209 (1994).
[2] J. D. Strachan, A. Bhattacharjee, D. J. Jassby, and H. H. Towner, Phys. Lett. A **66**, 295 (1978).
[3] A. L. Roquemore, R. C. Chouinard, M. Diesso, R. Palladino, J. D. Strachan, and G. D. Tait, Rev. Sci. Instrum. **61**, 3163 (1990).
[4] A. L. Roquemore, M. Bitter, L. C. Johnson, and S. von Goeler, Rev. Sci. Instrum. **68**, 544 (1997).
[5] L. C. Johnson, Rev. Sci. Instrum. **63**, 4517 (1992).
[6] J. M. Adams, O. N. Jarvis, G. J. Sadler, D. B. Syme, and N. Watkins, Nucl. Instrum. Methods Phys. Res., Sect. A **329**, 277 (1993).
[7] M. Riva, B. Esposito, D. Marocco, F. Belli, B. Syme, and L. Giacomelli, Fusion Eng. Des. **86**, 1191 (2011).
[8] T. Craciunescu, G. Bonheure, V. Kiptily, A. Murari, S. Soare, I. Tiseanu, V. Zoita, and JET EFDA Contributors, Nucl. Instrum. Methods Phys. Res., Sect. A **595**, 623 (2008).
[9] M. Ishikawa, T. Nishitani, A. Morioka, M. Takechi, K. Shinohara, M. Shimada, Y. Miura, M. Nagami, and Yu. A. Kaschuc, Rev. Sci. Instum. **73**, 4237 (2002).
[10] M. Ishikawa, T. Itoga, T. Okuji, M. Nakhostin, K. Shinohara, T. Hayashi, A. Sukegawa, and M. Baba, Rev. Sci. Instrum. **77**, 10E706 (2006).
[11] M. Ishikawa, M. Takechi, K. Shinohara, Y. Kusama, C. Z. Cheng, G. Matsunaga, Y. Todo, N. N. Gorelenkov, G. J. Kramer, R. Nazikian, A. Fukuyama, V. A. Krasilnikov, Yu. Kashuck, T. Nishitani, A. Morioka, M. Sasao, M. Isobe, and JT-60 Team, Nucl. Fusion **45**, 1474 (2005).
[12] P. Batistoni, B. Esposito, M. Martone, and S. Mantovani, Rev. Sci. Instrum. **66**, 4949 (1995).
[13] M. Cecconello, M. Turnyanskiy, S. Conroy, G. Ericsson, E. Ronchi, S. Sangaroon, R. Akers, I. Fitzgerald, A. Cullen, and M. Weiszflog, Rev. Sci. Instrum. **81**, 10D315 (2010).
[14] J.-G. Kwak, H. S. Kim, M. S. Cheon, S. T. Oh, Y. S. Lee, T. Terzolo, and KSTAR Team, Fusion Eng. Des. **109-111**, 608 (2016).
[15] Y. Izumi, H. Tomita, Y. Nakayama, S. Hayashi, K. Morishima, M. Isobe, M. S. Cheon, K. Ogawa, T. Nishitani, T. Naka, T. Nakano, M. Nakamura, and T. Iguchi, Rev. Sci. Instrum. **87**, 11D840 (2016).
[16] G. Q. Zhong, L. Q. Hu, N. Pu, R. J. Zhou, M. Xiao, H. R. Cao, Y. B. Zhu, K. Li, T. S. Fan, X. Y. Peng, T. F. Du, L. J. Ge, J. Huang, G. S. Xu, B. N. Wan, and EAST Team, Rev. Sci. Instrum. **87**, 11D820 (2016).
[17] Y. P. Zhang, J. W. Yang, Y. Liu, T. S. Fan, X. B. Luo, G. L. Yuan, P. F. Zhang, X. F. Xie, X. Y. Song, W. Chen, X. Q. Ji, X. Li, T. F. Du, L. J. Ge, B. Z. Fu, M. Isobe, X. M. Song, Z. B. Shi, Q. W. Yang, and X. R. Duan, Rev. Sci. Instrum. **87**, 063503 (2016).
[18] W. J. Capecchi, J. K. Anderson, P. J. Bonofiglo, J. Kim, and S. Sears, Rev. Sci. Instrum. **87**, 11D826 (2016).
[19] M. Cecconello, S. Sangaroon, M. Turnyanskiy, S. Conroy, I. Wodniak, R. J. Akers, G. Ericsson, and MAST Team, Nucl. Fusion **52**, 094015 (2012).
[20] L. Giacomelli, A. Hjalmarsson, H. Sjöstrand, W. Glasser, J. Källne, S. Conroy, G. Ericsson, M. Gatu Johnson, G. Gorini, H. Henriksson, S. Popovichev, E. Ronchi, J. Sousa, E. Sunden Andersson, M. Tardocchi, J. Thun, M. Weiszflog, and Contributors to the JET-EFDA Workprogram, Nucl. Fusion **45**, 1191 (2005).
[21] D. Marocco, B. Esposito, and F. Moro, J. Instrum. **7**, C03033 (2012).
[22] M. Sasao, M. Isobe, M. Osakabe, A. Taniike, T. Iguchi, H. Takada, T. Iida, and M. Wada, Fusion Eng. Des. **34**, 595 (1997).
[23] X-5 Monte Carlo Team, "MCNP—A general N-particle transport code, version 5," Volume I: Overview and Theory LA-UR-03-1987, 2003, updated, 2005.
[24] M. Isobe, H. Yamanishi, M. Osakabe, H. Miyake, H. Tomita, K. Watanabe, H. Iwai, Y. Nomura, N. Nishio, K. Ishii, J. H. Kaneko, J. Kawarabayashi, E. Takada, A. Uritani, M. Sasao, T. Iguchi, Y. Takeiri, and H. Yamada, Rev. Sci. Instrum. **81**, 10D310 (2010).
[25] K. Ogawa, M. Isobe, E. Takada, Y. Uchida, K. Ochiai, H. Tomita, A. Uritani, T. Kobuchi, and Y. Takeiri, Rev. Sci. Instrum. **85**, 11E110 (2014).
[26] H. Kawase *et al.*, "Evaluation of spatial resolution of neutron profile monitor in LHD," IEEE Trans. Plasma Phys. (published online).
[27] See https://www.hamamatsu.com/resources/pdf/etd/R11265U_H11934_TPMH1336E.pdf for the specification of H11934-100-10MOD.
[28] See http://www.hongsencable.com/pdf/01714670.pdf for the specification of 3D-FB cable.
[29] See https://www.tek.com/datasheet/digital-phosphor-oscilloscopes for the data sheet of DPO7000 series.
[30] See http://www.techno-ap.com/img/APV8102_14MWPSAGb.pdf for the specification of APV8102-14MWPSAGb.
[31] See http://www.techno-ap.com/img/APV3304.pdf for the specification of APV 3304.
[32] See https://www.matsusada.com/product/psel/dcps/handy/000002/ for the data sheet of P4K-80.
[33] See http://netgear.com/business/products/switches/smart/XS712T.aspx for the specification of XS712.
[34] M. Y. Tanaka, M. Aramaki, K. Ogiwara, S. Etoh, S. Yoshimura, and J. Varanjes, AIP Conf. Proc. **1061**, 57 (2008).
[35] See https://www.nfcorp.co.jp/english/sup/dl/manual/mi/e_wf1946b.pdf for the instruction manual of WF1964B.
[36] K. Ishii, K. Shinohara, M. Ishikawa, M. Baba, M. Isobe, A. Okamoto, S. Kitajima, and M. Sasao, Rev. Sci. Instum. **81**, 10D334 (2010).
[37] C. Konno, *Compendium of Neutron Beam Facilities for High Precision Nuclear Data Measurements*, IAEA-TECDOC-1743 (IAEA, Vienna, 2014), pp. 110–118, https://www-nds.iaea.org/publications/tecdocs/iaea-tecdoc-1743/.
[38] See https://eng.surugaseiki.com/Products/spec/Motorized+Stage/Motorized+Linear+Stage/X-Axis+Motorized+Stage/KXL06300/KXL06300-N2-F3C/pkey:X-Axis%20Motorized%20Stage%20%E2%96%A160 for the specification of KXL06300.
[39] See http://www.caen.it/csite/CaenProd.jsp?parent=14&idmod=632 for the specification of DT5751.
[40] See http://www.ni.com/ja-jp/support/model.ni-5772.html for the specification of NI-5772.
[41] See http://www.ni.com/ja-jp/support/model.pxie-7962.html for the specification of PXIe-7962.
[42] M. Baba, M. Takada, T. Iwasaki, S. Matsuyama, T. Nakamura, H. Ohguchi, T. Nakano, T. Sanami, and N. Hirakawa, Nucl. Instrum. Methods Phys. Res., Sect. A **376**, 115 (1996).
[43] I. Murata, *Compendium of Neutron Beam Facilities for High Precision Nuclear Data Measurements*, IAEA-TECDOC-1743 (IAEA, Vienna, 2014), pp. 110–118, https://www-nds.iaea.org/publications/tecdocs/iaea-tecdoc-1743/.
[44] I. Yamada, K. Narihara, H. Funaba, T. Minami, H. Hayashi, T. Kohmoto, and LHD Experiment Group, Fusion Sci. Technol. **58**, 345 (2010).
[45] T. Akiyama *et al.*, Fusion Sci. Technol. **58**, 352 (2010).
[46] M. Isobe *et al.*, Rev. Sci. Instrum. **85**, 11E114 (2014).